Medicine®

OPEN

Prediction of lung squamous cell carcinoma immune microenvironment and immunotherapy efficiency with pyroptosis-derived genes

Xiaheng Deng, MD[a], Zhibo Wang, MD[a], Yu Luo, MD[a] (iD), Zhihua Li, MPH[a], Liang Chen, MD[a,*]

Abstract

Lung squamous cell carcinoma (LUSC) is a common subtype of lung cancer that exhibits diverse pyroptosis regulatory patterns. Studies have highlighted the significance of pyroptosis in cancer invasion and immune responses. We aimed to explore the signatures of pyroptosis-related genes and their immune relevance in LUSC. Using The Cancer Genome Atlas (TCGA)-LUSC cohort and 5 gene expression omnibus (GEO) datasets, we performed consensus clustering based on 41 pyroptosis-related genes, and single sample gene set enrichment analysis (ssGSEA) was employed to calculate the infiltration levels of distinct clusters. A pyroptosis scoring scheme using the principal component analysis (PCA) method was used to quantify pyroptosis regulation in patients with LUSC and predict their prognosis. Four pyroptosis clusters were identified among 833 LUSC samples, which were associated with different Kyoto encyclopedia of genes and genome (KEGG) signaling pathways and tumor microenvironment infiltration features, and were highly consistent with 4 reported immune phenotypes: immune-responsive, immune-non-functional, immune-exclusion, and immune-ignorance. We then divided the patients into high- and low-pyroptosis score subgroups, and patients with higher scores were characterized by prolonged survival and attenuated immune infiltration. Moreover, higher scores were correlated with male patients, higher microsatellite instability, lower immune checkpoint inhibitor expression (such as CTLA-4 and GAL-9), and high mutation rates of typical mutated genes (e.g., TP53 and TTN). In particular, patients with lower pyroptosis scores showed better immune response to immune checkpoint inhibitor treatment. Pyroptosis regulatory patterns in the immune microenvironment can predict the clinical outcomes of patients with LUSC. Accurately quantifying the pyroptosis of individual patients will strengthen the understanding of heterogeneity within the LUSC tumor microenvironment infiltration areas.

Abbreviations: DEG = differentially expressed genes, GSDMD = gasdermin D, GSDME = gasdermin E, GSVA = gene set variation analysis, ICI = immune checkpoint inhibitors, IHC = immunohistochemistry, IPS = immunophenoscore, LUSC = lung squamous cell carcinoma, MSI = microsatellite instability, NK = natural killer, NSCLC = non-small cell lung cancer, PCA = principal component analysis, RFE = recursive feature elimination, ssGSEA = single sample gene set enrichment analysis, TCGA = the Cancer Genome Atlas, TIDE = tumor immune dysfunction and exclusion, TILs = tumor-infiltrating lymphocytes, TMB = tumor mutational burden, TME = tumor microenvironment.

Keywords: immune checkpoint inhibitor, immune microenvironment, lung squamous cell carcinoma, prognosis prediction, pyroptosis

1. Introduction

Pyroptosis is a type of an inflammatory programmed cell death characterized by membrane rupture, cellular swelling, cell extravasation, chromatin condensation, and DNA breakage, and plays a central role in provoking microbial infections and endogenous danger signals.[1] During inflammatory responses, gasdermin D (GSDMD)-mediated activation is regulated by caspases ¼/5/11,

as well as caspase 3 that induces GSDME-dependent activation, which consists of 2 main approaches of pyroptosis-facilitated cell death.[2–4] The activity of these regulators has a great impact on pyroptosis and their examination can improve the understanding of pyroptosis mechanisms in diverse diseases such as hepatitis,[5] neurodegeneration,[6] atherosclerosis,[7] and tumors.[8] However, studies have demonstrated that pyroptosis exerts dual effects on tumors: it directly suppresses tumor cell proliferation on the

---

*Correspondence: Liang Chen, Department of Thoracic Surgery, The First Affiliated Hospital of Nanjing Medical University, 300 Guangzhou Road, Nanjing 210000, China (e-mail: clbright0909@njmu.edu.cn).

one hand, while on the other hand it forms a microenvironment promoting cancer growth, invasion, and drug resistance.[9] An intensive investigation of genetic variations and expression perturbation will further elucidate cancer heterogeneity and identify pyroptosis-related therapeutic targets.[10]

Lung squamous cell carcinoma (LUSC), a predominant subtype of non-small cell lung cancer (NSCLC), has an unfavorable prognosis, with a <15% 5-year survival rate and limited therapy targets.[11] Accumulating studies have proven that immune checkpoint inhibitors (ICI) such as PD-1/PD-L1 and CTLA-4 have transformed therapeutic strategies for LUSC and significantly improved clinical outcomes in treatment-I patients with advanced cancer.[12] With an increased understanding of the role of the tumor microenvironment (TME) in tumorigenesis and metastasis, it was observed that tumor-infiltrating lymphocytes (TILs) constitute a critical approach for predicting the response to ICI treatments.[13,14] Indeed, PD-1 expression in tumor-infiltrating CD8+ T cells has been indispensable for PD-L1 ICI therapeutic efficacy in LUSC.[15,16] However, obvious heterogeneity of the TME may exist in LUSC, and their characteristics might influence LUSC response to ICI therapy. Herbst et al[17] classified NSCLC into 4 types based on the histological observations of the immune environment: immunological response, a non-functional immune response with decreased PD-L1 expression, immunological ignorance, and excluded immune infiltration. Another TME 4-type classification method for NSCLC was proposed by Teng et al,[18] which is unique and represents a state of PD-L1 expression induced by oncogenic mutations. Thus, there is an urgent need to elucidate immunophenotypic changes in the LUSC TME.

Recently, increasing evidence has demonstrated the interactions between TME-infiltrated immune cells and pyroptosis, creating an opportunity to turn "immune cold" tumor to "immune hot" tumor with the induction of immunogenic death of tumor cells.[19–21] Pyroptosis could strengthen various signaling pro-inflammatory pathways and "fire up" the TME to overcome the immune desert phenotype, thus promoting cancer cell death. Zhang et al[22] discovered that high expression of wild-type GSDME was associated with augmented TILs, including CD8+ T cells and natural killer (NK) cells. Meanwhile, the release of pyroptosis-produced cytokines might reform the TME and enhance tumor cell survival by evading immune surveillance.[14] For example, IL-1β release induced by pyroptosis may trigger the transport of myeloid cells into the TME and promote breast cancer proliferation and metastasis.[23] GSDMD-mediated pyroptosis has been found to assist NSCLC in evading the innate immune response through dysregulation of immunomodulatory factors.[24] However, these studies merely focused on limited pyroptosis factors that might exert a coordinated function with other pyroptosis genes. Currently, a growing number of high-throughput sequencing datasets offer a comprehensive approach to identify the association between multiple pyroptosis genes and TME cell infiltration characteristics, which will broaden our understanding of the role of pyroptosis in LUSC immunity.

In our study, we systematically appraised the linkage between 41 pyroptosis genes and TME characteristics in more than 830 LUSC samples from The Cancer Genome Atlas (TCGA) and Gene Expression Omnibus (GEO) databases. Four different pyroptosis-related immunoinfiltration patterns with consensus clustering were identified, which are strongly interrelated with the previously reported 4-phenotype immune infiltration features: immune-responsive, immune-ignorant, immune-nonfunctional, and immune-exclusion.[17,18] Finally, we established a scoring method to determine the role of pyroptosis in TME shifting and its potential to predict the response to ICI therapy. Our results provide new insights into pyroptosis in the heterogeneity of the cancer immune microenvironment and highlight its efficacy in cancer immunotherapy.

2. Methods

2.1. Data acquisition and sample collection

The RNA transcriptome sequences and corresponding clinicopathological data were collected from the public database TCGA portal (https://portal.gdc.cancer.gov/), which includes the data of 502 patients with LUSC and 49 normal tissue samples, and the NCBI GEO database (https://www.ncbi.Nlm.Nih.gov/geo/), including those from GSE17710 (N = 56),[25] GSE30219 (N = 61),[26] GSE37745 (N = 66),[27] GSE41271 (N = 80),[28] and GSE73403 (N = 69).[29] Fragments per kilobase of transcript per million mapped reads (FPKM) format sequencing data from TCGA dataset were transformed into transcripts per kilobase million (TPM) format. We used the "Combat" in *R* language "sva" package to remove batch effects among these platforms from multiple GEO cohorts. Somatic gene mutations and copy number variations in TCGA-LUSC sample data were obtained from the UCSC Xena database. The exclusion criteria were samples without information on survival times or outcomes, status, age, sex, grade, smoking status, or TNM classification; and patients who received any treatment or neoadjuvant therapy before surgery.

Varscan, a tool to detect variants (single nucleotide polymorphisms (SNPs) and indels) in next-generation sequencing data, was used to recognize somatic mutations in mutation annotation format files, which are tab-delimited files containing somatic and/or germline mutation annotations.[30] The *R* package "maftools" was used to visualize the mutations in top mutated genes and "Rcircos" was used to plot the copy number variation landscape of pyroptosis-related genes in human chromosomes.

To verify the expression of genes comprising the pyroptosis score in LUSC and normal tissues, we conducted an experimental validation using 3 LUSC patient specimens (tumor specimens and adjacent normal tissues) from patients who underwent pulmonary lobectomy from January 2020 to December 2020 at the First Affiliated Hospital of Nanjing Medical University. During recruitment before surgery, patients provided written informed consent by trained interviewers through face-to-face interviews. An independent pathological review confirmed that the features of tumor specimens were histologically consistent with the pathological features of LUSC. The Nanjing Medical University Ethics Committee approved this study and its design, and all patients provided written informed consent.

2.2. Consensus clustering of 41 pyroptosis-related genes

In total, 41 pyroptosis-related genes were obtained from the MSigDB gene set (https://www.gsea-msigdb.org/gsea/msigdb/, v7.1) and from previous studies.[8,10,31] Due to the lack of normal LUSC tissue data in the GEO datasets, only TCGA-LUSC data were calculated to identify the differential expression of these pyroptosis-related genes using the R package "limma". A protein-protein interaction (PPI) network for these pyroptosis-related genes was constructed using the STRING website (https://string-db.org/), and the *R* package "reshape2" was used to draw a co-expression network.

Samples from TCGA and GEO cohorts were classified into different subgroups using consensus clustering, which was performed using the K-means algorithm with Spearman distance. The maximum cluster number was 10, and the final cluster number was determined using the consensus matrix and cluster consensus score using the R package "ConsensusClusterPlus". Repetition was performed 1000 times to guarantee the stability of the classification.

2.3. Gene set variation analysis (GSVA) and immune cell infiltration estimation by single sample gene set enrichment analysis (ssGSEA)

GSVA was conducted by the *R* package "GSVA" to investigate the Kyoto Encyclopedia of Genes and Genomes (KEGG)

discrepancy among the 4 pyroptosis clusters. The KEGG signatures "c2.cp.kegg.v7.2. symbols" were acquired from the Hallmarker-geneset in the MSigDB and the annotation was achieved with the *R* package "clusterProfiler" with a cutoff value of *P* < .05. We then utilized ssGSEA to quantify the infiltration of 23 immunocytes in the TME.[32] The ESTIMATE algorithm was used to quantify the immune and stromal scores which were combined to infer tumor purity.[33]

2.4. Identification of differentially expressed genes (DEGs) and construction of a pyroptosis score

The *R* package "limma" package was used to detect DEGs among these 4 pyroptosis clusters, and a Venn diagram was constructed to view the number of overlapping genes among these DEGs. The cutoff of the DEGS was set at adjusted *P* < .001. The LUSC samples were then classified into 3 subgroups based on the transcriptomic landscape of the 17 intersecting genes. Using recursive feature elimination (RFE) with a 10-fold cross validation method in the *R* package "caret," the genes with a significant prognostic value, which were analyzed by a univariate Cox regression model, were examined further. Using principal component analysis (PCA), the selected genes were divided into principal components 1 and 2 and the pyroptosis score $= \sum (PC1_i + PC2_i)$. The advantage of this method was that it focused mainly on the score of genes that were positively or negatively correlated to the largest block, while downweighing contributions from genes that were isolated from other members. Kaplan–Meier survival curves were used to assess the ability of the pyroptosis score to discriminate between different subtypes of patients. Clinical parameters such as age, sex, TNM stage, and pyroptosis score were applied to univariate and multivariate Cox regression analyses using a backward stepwise Cox proportional hazard model. The coefficients of each parameter derived from the multivariate analysis were used to construct a prognostic nomogram. The survival status for patients at 1, 3, and 5 years was used as the endpoint parameters for the development of the nomogram[34] with the *R* package "regplot". The discrimination and calibration of the nomogram for the endpoint index were measured using the concordance index (C-index) and a calibration plot comparing the expected and observed survival probabilities, respectively.

2.5. Quantify the immune response prediction ability by tumor immune dysfunction and exclusion (TIDE) and immunophenoscore (IPS)

The TIDE algorithm was applied to imply tumor immune evasion possibilities, including the exclusion and dysfunction of TILs affected by immunosuppressive factors.[35] The IPS, a predictor of ICI therapy, especially for anti-CTLA-4 and anti-PD-L1 therapies, was calculated based on the sum of the weighted averaged Z score of immune-related genes grouped into 4 classes: effector cells, immunosuppressive cells, MHC molecules, and immunomodulators.

2.6. Experimental validation

Frozen sections cut at 5 μm thickness were stained for immunohistochemistry (IHC). IHC was performed using antibodies against ABCF3 (1:200, bs-7941R; Bioss, Beijing, China), FGFR2 (1:200, bs-7941R; Bioss), IGSF11 (1:50, 14003-1-AP; Proteintech, Wuhan, China), P2RY6 (1:100, ab92504; Abcam, Cambridge, UK), and SOX2 (1:100, ab92497; Abcam). Slides were incubated overnight with the primary antibody at 4°C and horseradish peroxidase (HRP) secondary antibody (KIT-5005; MaxVision, Fuzhou, China) for 30 minutes at 37°C. Then, the samples were incubated with a 3,3′-diaminobenzidine

tetrahydrochloride (DAB) Kit (DAB-1031; Maxim, Fuzhou, China) for 2 minutes at 37°C, followed by hematoxylin counterstaining at room temperature. The Human Protein Atlas database was utilized to determine expression levels of proteins (ACSL5, DVL3, LAMC2, NTS, SOX21, and SPAST), for which we could not obtain antibodies. No staining indicated the absence of protein expression. The presence of staining in cells was deemed positive irrespective of the proportion or intensity. Moreover, the mRNA expression levels of the candidate genes were further validated using the data in our own RNA-seq databases, including that of 19 paired LUSC samples.[36]

2.7. Statistical analysis

R software (v4.0.3) was used for the statistical analysis. The correlation between the mutant genes and TMB was determined using the Mann–Whitney *U* test. The enriched functions associated with DEGs were determined using the *R* package "clusterProfiler." Spearman's correlation and bi-directional detection were computed using the Cor.test function in *R*. The survival-cutpoint function from the *R* package "survival" was applied to stratify the samples into distinct pyroptosis scores. Two-tailed *P* < .05 was considered statistically significant for all comparisons.

3. Results

3.1. Landscape of expression and genetic variations of pyroptosis-related genes in LUSC

The expression of 41 pyroptosis-related genes was explored in 502 LUSC and 49 normal samples from TCGA dataset, and 35 genes were identified as DEGs. As shown in Figure 1A, the expression of *BAX*, *CASP3*, *CHMP4B*, *CHMP4C*, *CYCS*, *GSDME*, *HMGB1*, *TP53*, *TP63*, *AIM2*, *CASP6*, *GSDMB*, *GSDMC*, and *NLRP7* was upregulated, whereas that of another 21 genes (*CASP1*, *CASP4*, *CASP5*, *CHMP2B*, *CHMP6*, *CHMP7*, *GSDMD*, *GZMB*, *IL18*, *IL1B*, *IRF1*, *IRF2*, *CASP9*, *IL6*, *NLRP1*, *NOD1*, *NOD2*, *PRKACA*, *NLRP3*, *TIRAP*, and *TNF*) was downregulated in malignant group. We then constructed a PPI network to determine the interactions between these pyroptosis-related genes with a minimum required interaction score of 0.700 (Fig. 1B). With the exception of *PYCARD*, pyroptosis-related genes including *NLRP3*, *GSDMD*, *NLRP1*, *CASP1*, *CASP3*, *TP53*, and *CASP5* were all differentially expressed in LUSC tissues and were highly interrelated with other genes in this network. Moreover, as shown in Figure 1C, *NLRP3*, *AIM2*, *CASP4*, and *CASP5* were positively coexpressed, whereas TP63 and CYCS showed negative coexpression trends within the correlation network.

Furthermore, we investigated pyroptosis-related gene mutations in TCGA samples. As shown in Figure 1D, since TP53 is well known to be frequently mutated in LUSC, TP53 mutations were excluded, and it was found that 113 of 491 (23.01%) samples demonstrated genetic mutations. Of these, *NLRP3* showed the highest frequency of mutations, and missense mutations were the most common. The copy number variation (CNV) alteration frequency results demonstrated that 12 genes had copy number deletions, whereas *AIM2*, *CHMP6*, *GSDMD*, *GSDMC*, and *TP63* showed widespread CNV amplifications (Fig. 1E). The locations of the CNV alterations in the 28 pyroptosis-related genes are shown in Figure 1F.

3.2. Identification of LUSC classification pattern mediated by pyroptosis-related genes

To further elucidate the potential LUSC classification pattern, 5 GEO datasets containing LUSC cases with overall survival (OS) data and clinical information were examined. Kaplan–Meier
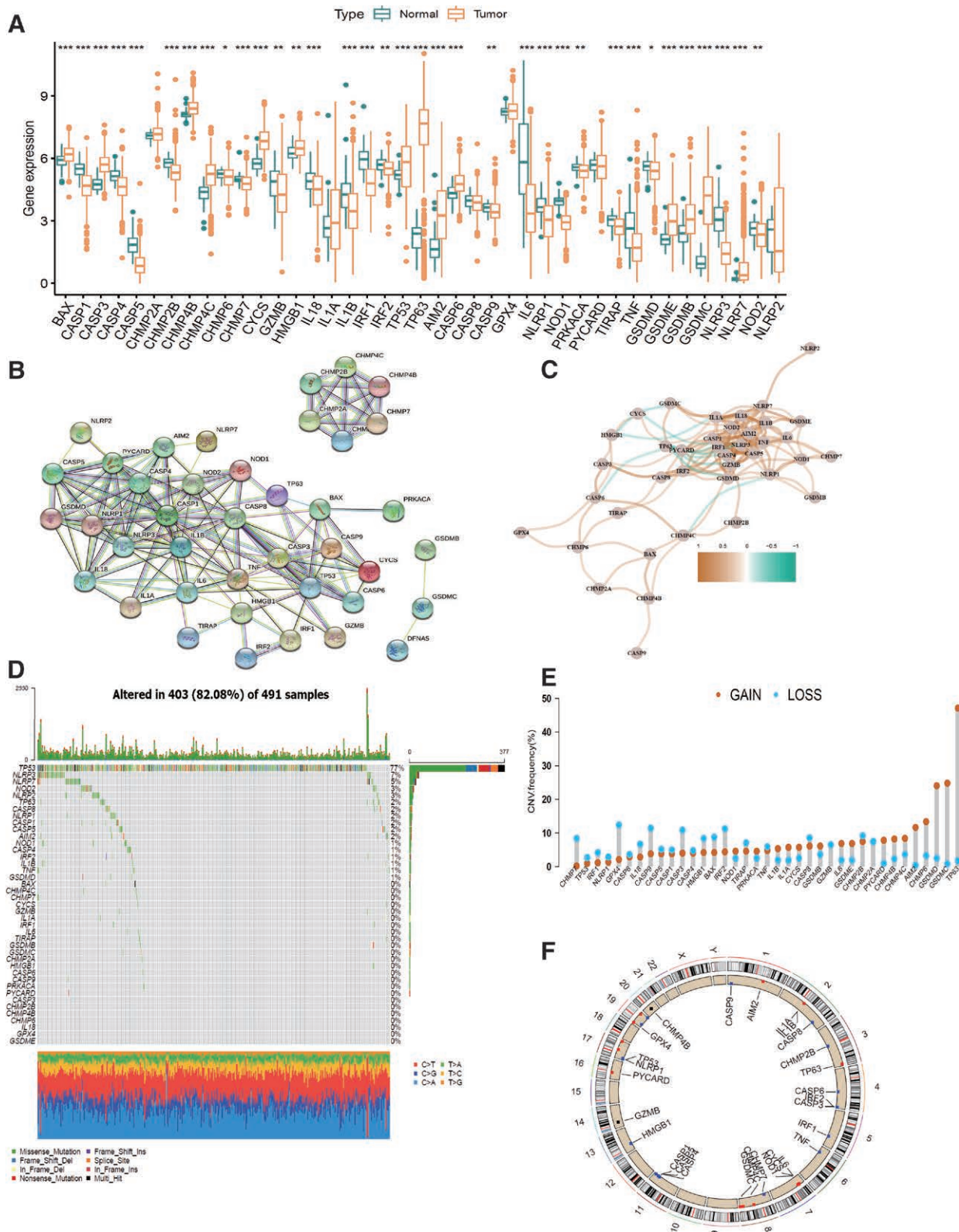
Figure 1. The landscape of expression and genetic variations of pyroptosis-related genes in LUSC. (A) The expression of 41 pyroptosis-related genes in LUSC tumor and normal samples. Yellow: Tumor, Green: Normal. *P < .05, **P < .01, ***P < .001. (B) A PPI network demonstrating the interactions of the pyroptosis-related genes (interaction score = 0.7). (C) The correlation network of the pyroptosis-related genes. Yellow: positive correlation; Green: negative correlation. The depth of the colors imitates the strength of the correlation. (D) The landscape of mutation profiles in 491 LUSC patients from TCGA dataset. The left panel indicates the mutation frequency ordered by gene frequencies. The right panel presents different mutation categories. (E) CNV frequency of pyroptosis-related genes in TCGA cohort. The height of the columns showed proportions of CNV deletion (Blue) and CNV amplification (Brown). (F) The location of CNV alteration of pyroptosis-related genes on chromosomes. CNV = copy number variations, LUSC = lung squamous cell carcinoma, PPI = protein-protein interactions, TCGA = The Cancer Genome Atlas.

curves were constructed to screen for pyroptosis-related genes with prognostic value. The elevated expression of *BAX* (*P* = .048), *TP63* (*P* = .018), *NLRP2* (*P* = .043), *CHMP6* (*P* = .035), *GZMB* (*P* = .024), *CYCS* (*P* = .002), *GSDMC* (*P* = .038), and *CASP3* (*P* = .018) was found to represent a better survival rate; nevertheless, the high expression of *NOD2* (*P* < .001), *NOD1* (*P* = .036), *NLRP7* (*P* = .027), *NLRP3* (*P* = .012), *IRF1* (*P* = .013), *IL6* (*P* < .001), *IL1B* (*P* < .001), *IL1A* (*P* < .001), *CASP9* (*P* = .019), *GSDMD* (*P* = .001), *GSDME* (*P* = .002), *CHMP2B* (*P* < .001), *CHMP4C* (*P* < .001), and *CASP5* (*P* = .019) suggest a poor prognosis (see Figure S1, Supplemental Digital Content 1, http://links.lww.com/MD/H203, which illustrates overall survival in different pyroptosis-related gene expressions). Next, a summarized network of pyroptosis-related genes that might be involved in canonical and non-canonical inflammasome pathways was created, and the gene correlations and prognostic values were panoramically illustrated. The results indicated that canonical and non-canonical inflammasome pathways might not function independently but interact with each other in cancer deterioration (Fig. 2A). Based on the consensus clustering of 41 pyroptosis-related genes, we identified 4 classification patterns: 328 samples in ClusterA, 72 samples in ClusterB, 164 samples in ClusterC and 269 samples in ClusterD (Fig. 2B). Prognostic analysis showed a significant survival advantage in ClusterD and a relatively worse survival in ClusterC (*P* = .005, Fig. 2C). Moreover, as shown in Figure 2D, prominent variations in expression were observed among these pyroptosis clusters. The expression of *CASP4*, *CASP5*, *IL1A*, *IL1B*, *IRF1*, *AIM2*, *IL6*, *TNF*, *NLRP3*, *NLRP7*, and *NOD2* is significantly diminished in ClusterD; *IL1A* and *TP63* expression is significantly mitigated in ClusterB, and *CASP5*, *IL1A*, *IL1B*, *IRF1*, *AIM2*, and *IL6* expression is notably ameliorated in ClusterC.

GSVA was conducted to further delineate the molecular mechanisms underlying distinct pyroptosis expression patterns, and KEGG heatmaps were constructed to provide a more intuitive interpretation of clustering differences. The enrichment pathways of ClusterA are principally associated with innate immune processes and stromal formation, such as focal adhesion (Fig. 2E and G). ClusterC is significantly associated with immune signaling processes such as NOD-like receptor signaling, Toll-like receptor signaling, RIG-I-like receptor signaling pathways, cytokine-receptor interaction, T cell receptor signaling pathway, and natural killer cell-mediated cytotoxicity (Fig. 2F and J). ClusterD is enriched mainly in the Hedgehog signaling pathway and basal cell carcinoma (Fig. 2I). However, ClusterB is highly enriched in primary immunodeficiency and metabolic diseases, such as type I diabetes and autoimmune thyroid disease (Fig. 2E, H, and I). In particular, compared to clusters A, C, and D, ClusterB presents a significantly downregulated activity of oncogenic pathways including the P53 signaling pathway, MAPK signaling pathway, Wnt signaling pathway, ErbB signaling pathway, and other pathways in malignancy such as basal cell carcinoma, small cell lung cancer, and glioma (Fig. 2E, H, and J).

3.3. Immune infiltration landscape characterization of distinct pyroptosis clusters

Previous studies have shown that the classification of various types of TME in LUSC is primarily correlated with the distribution of tumor immune cell infiltrates and the expression of immune checkpoints such as PD-L1. ssGSEA was used to generate a heatmap that visualizes the abundance of 23 infiltrating immunocytes from different pyroptosis clusters (Fig. 3A). As shown in Figure 3A and B, activated B cells, activated CD4 cells, activated CD8 cells, and natural killer T cells, which mainly exert anti-tumor functions, are significantly concentrated in both clusters B and C. In ClusterD, the population of most of these

23 infiltrating cells are diminished, which obviously represents the immune-desert landscape, except for CD56 bright natural killer cells, the populations of which are remarkably downregulated in ClusterB. The immune infiltration pattern in ClusterA shows a modest expression level compared to the other clusters. In addition, we examined the PD-L1 expression level in multiple pyroptosis clusters and found that ClusterC shows a notably elevated level of PD-L1, followed by clusters B and A (Fig. 3C). As expected, ClusterD has the lowest PD-L1 level.

To further determine whether the abundance of immune cells is retained in the tumor center or the stroma surrounding the tumor parenchyma, the ESTIMATE algorithm was used to calculate the immune score and tumor purity of the 4 pyroptosis clusters (Fig. 3D and E). The results demonstrated that ClusterB has the highest immune score but the lowest tumor purity suggesting that tumors in ClusterB might be surrounded by more non-tumor ingredients, especially non-infiltrating immune cells or stromal cells. However, ClusterD possesses the lowest stromal and immune scores and the highest tumor purity, indicating its immune-desert phenotype. Thus, the 4 pyroptosis-related clusters were categorized by distinct immune infiltration patterns: ClusterA is an immune non-functional phenotype characterized by immune cell infiltration with low PD-L1 expression; ClusterB is characterized by immune infiltration at the tumor margin (immune-exclusion); ClusterC is immune-responsive with activated immune infiltration and increased PD-L1 expression; and ClusterD is as an immune-ignorant phenotype with no immune infiltration.

3.4. Development of a scoring method based on pyroptosis regulatory patterns

DEGs reflect the inherent discrepancy within the 4 pyroptosis clusters and represent critical discriminating indicators when comparing the clusters. A Venn diagram was used to ascertain the overlapping DEGs, and 17 DEGs representing different regulatory patterns were identified (Fig. 4A). GO and KEGG analyses showed that these 17 DEGs are mainly enriched in signaling pathways regulating the pluripotency of stem cells, positive regulation of intracellular transport, organophosphate biosynthetic process, and neuron projection morphogenesis (see Figure S2A, Supplemental Digital Content 2, http://links.lww.com/MD/H204, which shows KEGG and GO enrichment analysis of 17 intersected DEGS). Furthermore, 12 genes were identified with prognostic values using univariate Cox regression analysis (Table 1). Based on these prognostic gene expressions, we used a consensus clustering method, and 3 transcriptomic phenotypes were acquired (Fig. 4B). We found that the expression of *FGFR2*, *SOX2*, *IGSF11*, *DVL3*, *NCBP2*, *ABCF3*, *SOX21*, *NTS*, and *SPAST* were critically suppressed in gene-C2, whereas they were highly expressed in gene-C3. In gene-C1, *NTS* also showed a diminished expression. Conversely, *ACSL5*, *LAMC2*, and *P2RY6* were upregulated in gene-C2 but downregulated in gene-C3 (Fig. 4C). Moreover, obvious prognostic differences were observed among the 3 pyroptosis gene subgroups. It was shown that gene-C3 is correlated with better outcomes, whereas gene-C2 demonstrated a relatively worse prognosis (Fig. 4D, *P* = .003). As shown in Figure 4E, we also examined the expression levels of the 41 pyroptosis-related genes, and significant expression differences were observed among the 3 pyroptosis gene subgroups.

To apply these classifications to the clinical therapy of LUSC and to quantify the degree of pyroptosis, we constructed a scoring method based on 12 prognostic pyroptosis signature genes (Table 1). We first examined the pyroptosis score in pyroptosis and gene clusters, and significant results were observed in these correlation analyses, indicating that the pyroptosis score could serve as an explicit cluster-distinguishing factor (Fig. 4F and G). Additionally, we divided the patients into high and low pyroptosis scores with
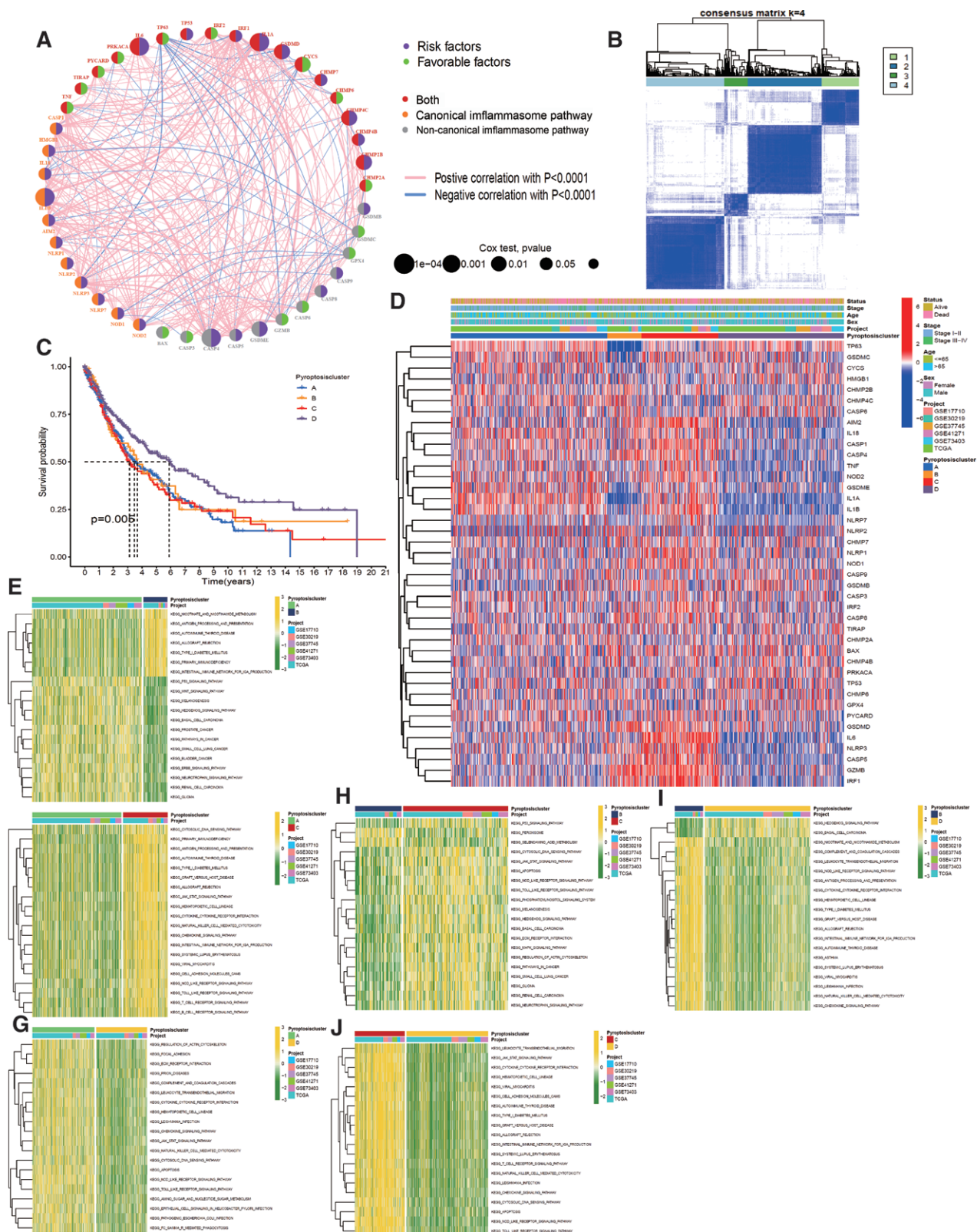
Figure 2. LUSC classification pattern mediated by pyroptosis-related genes and relevant KEGG pathway enrichment. (A) The interaction of 41 pyroptosis regulators expressions in LUSC. The pyroptosis-related genes involving inflammasome pathways are shown on the left side of the circles. Yellow: canonical inflammasome pathway; Grey: non-canonical inflammasome pathway; Red: both inflammasome pathways. The lines represent the interaction of each pyroptosis gene and the size of the circles show the prognosis effect scaled by the P-value. Green: defensive factors for patient survival; Purple: risk factors for patients' survival. (B) The consensus score matrix of all samples when k = 4 in TCGA and GEO cohorts (GSE17710, GSE30219, GSE37745, GSE41271, and GSE73403). (C) Overall survival curves of the 4 pyroptosis clusters based on 833 patients with LUSC (Log-rank test, P = .005). (D) A heatmap was used to visualize the variant pyroptosis-related gene expression among distinct pyroptosis clusters. Clinicopathological information including age, sex, stage, and survival status is revealed in the above annotations. Red: high expression; blue: low expression. (E–J) These heatmaps showed the KEGG pathway differences analyzed by GSVA between every 2 pyroptosis-related clusters with Bayes moderation. (E) A vs B; (F) A vs C; (G) A vs D; (H) B vs C; (J) C vs D; (I) B vs D. Yellow embodied the high expression and green embodied the low expression. GEO = gene expression omnibus, GSVA = gene set variation analysis, KEGG = Kyoto Encyclopedia of Genes and Genomes, LUSC = lung squamous cell carcinoma, TCGA = The Cancer Genome Atlas.
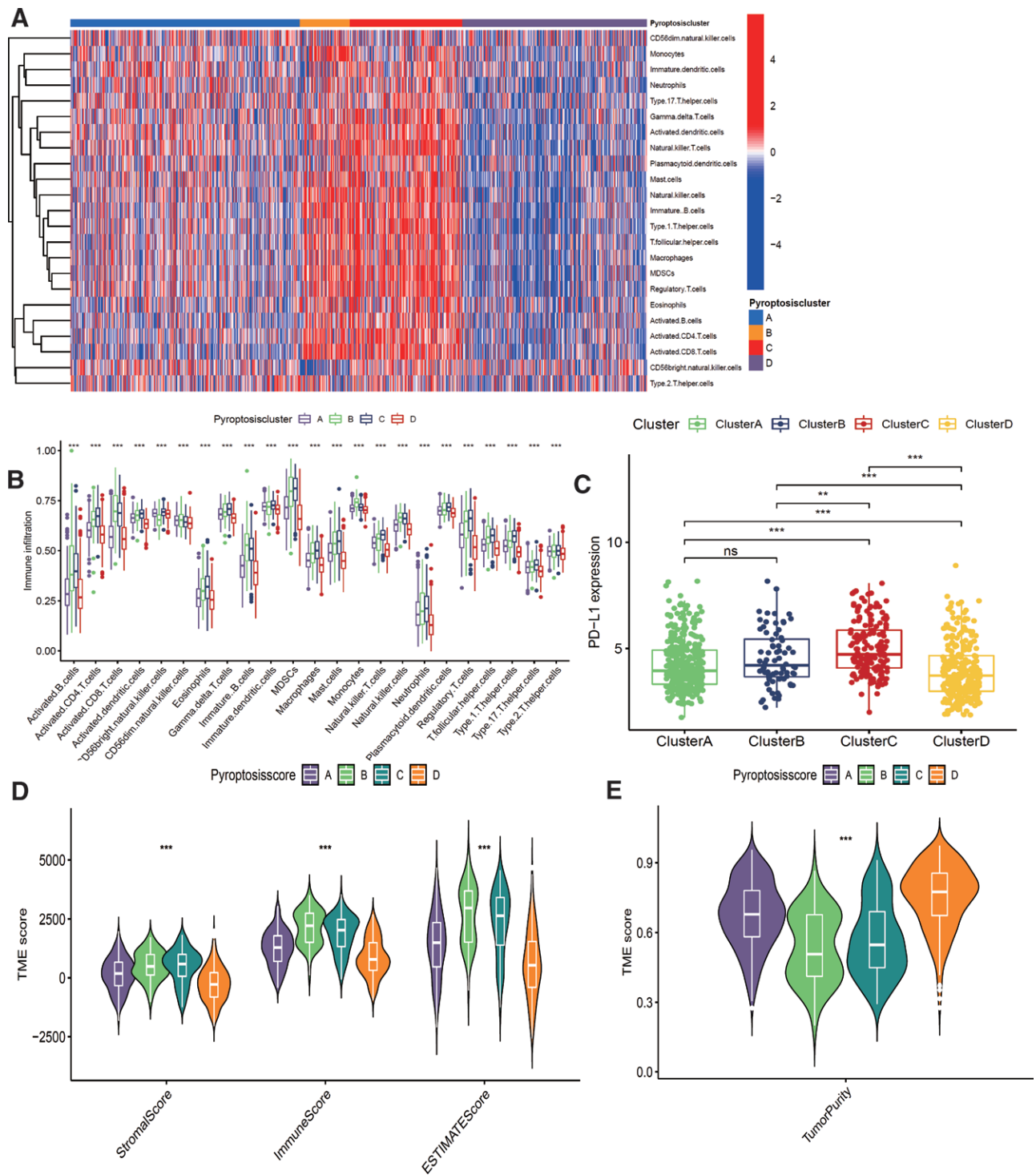
Figure 3. Immune microenvironment infiltration landscape characterization of distinct pyroptosis clusters. (A) A heatmap was used to visualize immune infiltrating cell discrepancy among the 4 pyroptosis clusters. Red embodies high expression and blue embodies low expression. (B) The fraction of TILs among pyroptosis clusters with the ssGSEA algorithm. The line embodies the median value. The scattered dots represent distinct immune cell expression values. (C) Comparison of PD-L1 expression level across 4 pyroptosis-related clusters. (D–E) The stromal score, immune score, ESTIMATE score (D) and tumor purity (E) of 4 clusters were analyzed and plotted. *$P < .05$, **$P < .01$, ***$P < .001$, *****$P < 1 × 10^{-5}$. ssGSEA = single sample gene set enrichment analysis, TILs = tumor-infiltrating lymphocytes.

the best cut-off value of –0.352. Next, we analyzed immunogenomic profiling of patients with LUSC using ssGSEA and classified them into immunity-high and immunity-low subtypes to associate the pyroptosis regulatory TME patterns (Fig. 4H). To visualize the multi-stage design of the quantification of pyroptosis regulation, we illustrated an alluvial diagram to unfold the process of pyroptosis score construction with immune infiltration

features (Fig. 4I). The results indicated that pyroptosis-ClusterA, classified as gene-C3, is mostly linked to a low immunity level. Pyroptosis-ClusterB is assembled mainly in gene-C1 and -C2 and presents a high immunity level, and pyroptosis-ClusterB, which is simultaneously exhibited in gene-C3, exhibits a restrained immunity. Notably, samples from pyroptosis-ClusterB were significantly associated with a lower pyroptosis score.
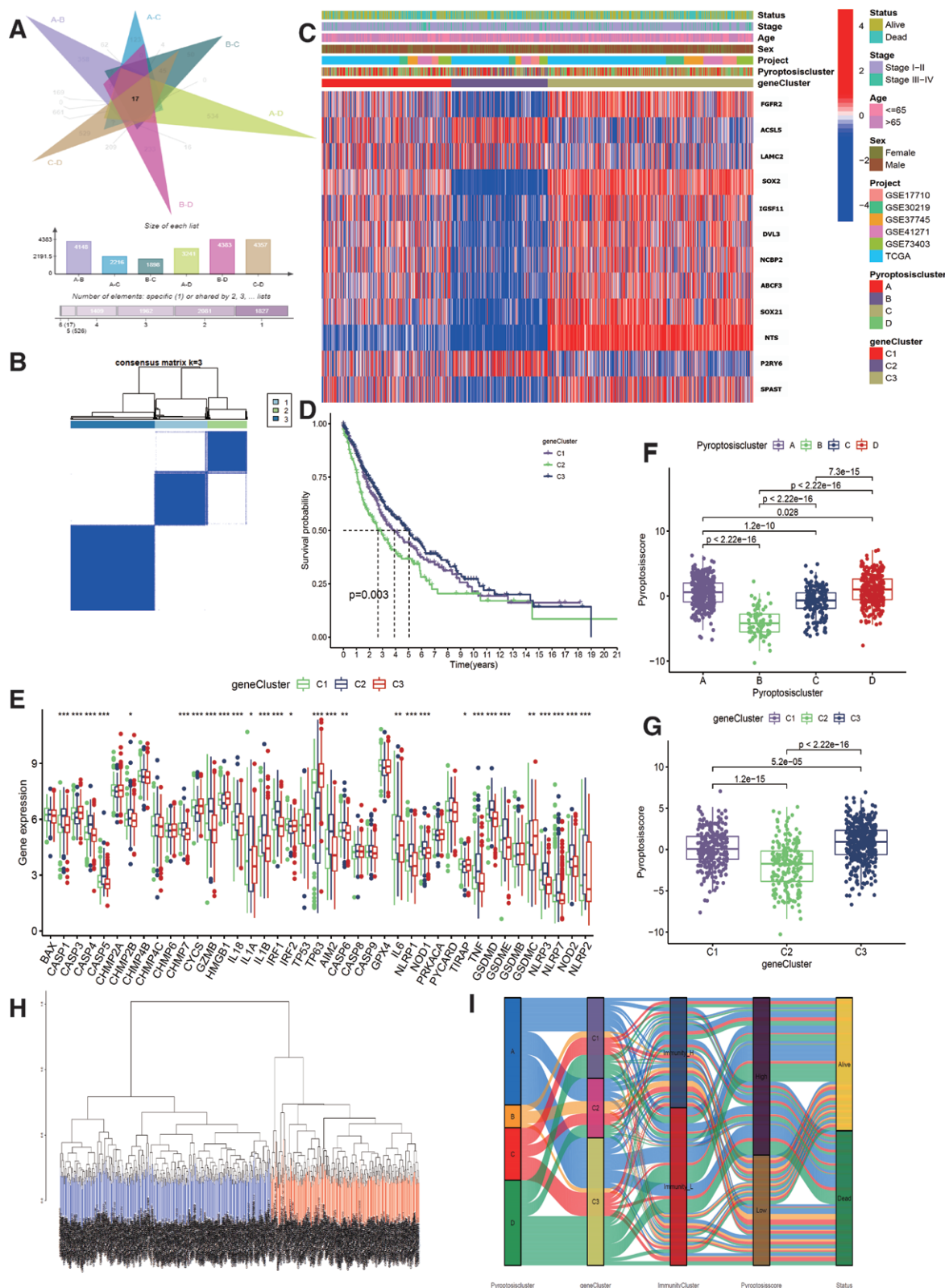
Figure 4. Construction of a scoring method based on pyroptosis regulatory patterns. (A) 17 pyroptosis cluster DEGs among the 4 clusters were shown in the Venn diagram. (B) The consensus score matrix of all samples when k = 3 in TCGA and GEO cohorts (GSE17710, GSE30219, GSE37745, GSE41271, and GSE73403) based on the 17 DEGs. (C) 12 DEGs identified using prognostic value by univariate Cox regression analysis in 3 gene clusters were shown in the heatmap. Clinicopathological information including age, sex, stage, and survival status were revealed in the above annotations. Red: high expression; blue: low expression. (D) Kaplan–Meier curves show overall survival of the patients in 3 gene clusters (Log-rank test, P = .003). € Variant expression of 41 pyroptosis-related genes among the 3 gene clusters. The line embodies the median value. The scattered dots represent distinct pyroptosis gene expression levels. *P < .05, **P < .01, ***P < .001. (F–G) Distribution of pyroptosis score in the different pyroptosis clusters (F) and gene clusters (G). The differences amid every 2 groups were compared using the Kruskal–Wallis H test. Precise P values are shown in the graph. (H) Totally, 833 samples were divided into immunity-high level and immunity-low level according to the ssGSEA analysis. Red: immunity-high; Blue: immunity-low. (I) Alluvial diagram of pyroptosis clusters and gene clusters in groups with different immunity level, pyroptosis score, and survival status. DEGs = differentially expressed genes, GEO = gene expression omnibus, ssGSEA = single sample gene set enrichment analysis, TCGA = The Cancer Genome Atlas.

The overlapping differential expressing genes with a significant prognostic impact with a univariate Cox regression model.

Gene	*P* value	HR (95% CI)
FGFR2	.001	0.879 (0.813–0.950)
ACSL5	.026	1.097 (1.011–1.190)
LAMC2	.005	1.090 (1.026–1.158)
SOX2	.002	0.929 (0.891–0.969)
IGSF11	.011	0.897 (0.825–0.976)
DVL3	.043	0.886 (0.788–0.996)
NCBP2	.047	0.867 (0.753–0.998)
ABCF3	.035	0.855 (0.738–0.989)
SOX21	.027	0.939 (0.888–0.993)
NTS	<.001	0.950 (0.924–0.976)
P2RY6	.021	1.130 (1.019–1.253)
SPAST	.003	0.818 (0.717–0.933)

CI = confidence interval, HR = hazard ratio.

3.5. Pyroptosis score association with LUSC clinical characteristics and TME alterations

To evaluate the prognostic ability of the pyroptosis score in predicting the outcomes of patients with LUSC, a Kaplan–Meier curve was constructed, and patients with a low pyroptosis score were meaningfully related with a worse prognosis, as expected (*P* = .009, Fig. 5A). We further explored the association between clinical characteristics and pyroptosis score subgroups, and the results indicated that males had a higher pyroptosis score than females (Fig. 5B and C). However, age and TNM stage did not demonstrate any association with pyroptosis scores (see Figure S2B–G, Supplemental Digital Content 2, http://links.lww.com/MD/H204, which demonstrated the association between pyroptosis score and clinical features). Further stratified survival analysis showed that for both female and male patients aged > 65 years, a high pyroptosis score was significantly associated with a better prognosis. Nonetheless, patients with early stage LUSC (stage I-II) with a high pyroptosis score suffer from a poor prognosis (Fig. 5D–G; see Figure S2H–I, Supplemental Digital Content 2, http://links.lww.com/MD/H204, which illustrates overall survival curves based on clinical features). Moreover, univariate and multivariate regression analyses revealed that age, T stage, and pyroptosis score could serve as independent predictors affecting the prognosis of patients with LUSC (Fig. 5H and I).

We then built a prognostic nomogram integrating the pyroptosis score and clinicopathological variables such as age and TNM stage to strengthen the predictive ability in patients with LUSC (Fig. 5J). Survival status at 1, 3, and 5 years was used as a parameter of clinical outcome. The calibration plots were highly consistent with the OS predictions and the actual observations of the 1-, 3-, and 5-year survival rates, and the results of receiver operating characteristic (ROC) curves confirmed the prediction advantage of this scoring scheme (1-year area under the curve (AUC) = 0.620, 3-year AUC = 0.660, 5-year AUC = 0.656; Fig. 5K and L).

According to the aforementioned results, the pyroptosis score is considered a good indicator for clinical prediction. We then investigated the role of the pyroptosis score in TME alterations. We first inspected the correlation between pyroptosis and infiltration scores in the LUSC microenvironment. ESTIMATE scores showed that stromal and immune scores were attenuated as pyroptosis score increased (Fig. 5M). The abundance of infiltrating immunocytes was evaluated using the pyroptosis score. Identical to our prediction, almost all the immune infiltration subtypes were negatively related with pyroptosis scores, such as activated B cells, activated CD4+ T cells, activated CD8+ T cells, and natural killer T cells (Fig. 5N). The type 2 T helper cells showed no correlation with pyroptosis scores. To further clarify

the immune cell variance from different pyroptosis score subgroups, a heatmap was generated to show the infiltrated immunocyte abundance according to the ESTIMATE and pyroptosis scores (Fig. 5O). The results clearly showed that low-score group had a more active immune response than high-score group. Tumors could be referred to as "immune-hot" and "immune-cold" depending on their TME infiltration cells, which showed different responses to immunotherapy.[21] Therefore, as indicated, low-score group could be classified into "immune-hot" and high score group was evidently "immune-cold" subgroup.

3.6. The role of pyroptosis score in predicting ICI immunotherapy

Accumulating evidence has shown that genomic somatic mutations, tumor mutational burden (TMB), and microsatellite instability (MSI) might serve as biomarkers for ICI immunotherapy outcomes, similar to immune cell infiltration. The distribution of mutated genes was appraised individually from high and low pyroptosis score groups, and low pyroptosis score group was shown to exhibit 100% mutation frequencies (Fig. 6A). Significantly mutated gene landscapes showed that *TP53*, *TTN*, and *CSMD3* retain elevated somatic mutation rates in high pyroptosis score group (low vs high, 62% vs 78%, 62% vs 70%, and 35% vs 41%, respectively). Alternatively, *MUC16* and *RYR2* mutations were more frequent in low score group (39% vs 34% and 38% vs 31%, respectively). Missense mutations remain the most prevalent mutation type in all frequently mutated genes. Moreover, we explored the TMB and MSI of different pyroptosis scores in TCGA cohort and discovered that lower score group had a higher MSI, whereas no significant results were observed for TMB (Fig. 6B–E). We also found a connection between pyroptosis clusters and MSI, which suggested that pyroptosis-ClusterD with the highest pyroptosis score has the highest MSI, whereas pyroptosis-ClusterB with the lowest score is associated with the lowest MSI (*R* = −0.21, *P* < .001). Consistent with previous studies, prognosis analysis demonstrated that patients with LUSC with higher TMB and MSI had a better prognosis (*P* < .001, *P* = .024, Fig. 6F and G). In addition, we combined TMB and MSI with pyroptosis scores and classified them into 4 components (Fig. 6H and I). We found that patients with both high TMB and pyroptosis scores had a significantly better prognosis than patients with low TMB and pyroptosis scores. Reciprocally, the combination of MSI and pyroptosis scores did not demonstrate a significant outcome prediction. Considering these results, the pyroptosis score might be a valuable predictor of the survival of patients with LUSC. When combined with TMB, the pyroptosis score takes a step further in improving the prediction performance compared to the pyroptosis score applied alone.

ICI treatment, represented by PD-L1 and CTLA-4 inhibitors, is ubiquitously used in NSCLC therapy. We first checked the expression variation of immune checkpoints according to the pyroptosis scores and found that except for PD-L1, CTLA-4, GAL-9, and LAG-3 were highly expressed in high pyroptosis score group, suggesting a better response to immunotherapy (Fig. 6J). Considering the tight linkage between pyroptosis scores and LUSC microenvironment, emerging indicators of immunotherapy such as tumor immune dysfunction and exclusion (TIDE) and immunophenoscore (IPS) were utilized in TCGA cohort to predict the response to ICI therapy. Our results showed that TIDE was negatively correlated with the pyroptosis score. Moreover, high pyroptosis score group showed higher immune exclusion and lower immune dysfunction (Fig. 6K–M). We further gauged the connection between the pyroptosis score and ICI therapy response with anti-CTLA4 and anti-PD-L1 treatment. The IPS results showed that for patients who did not receive immune therapy,
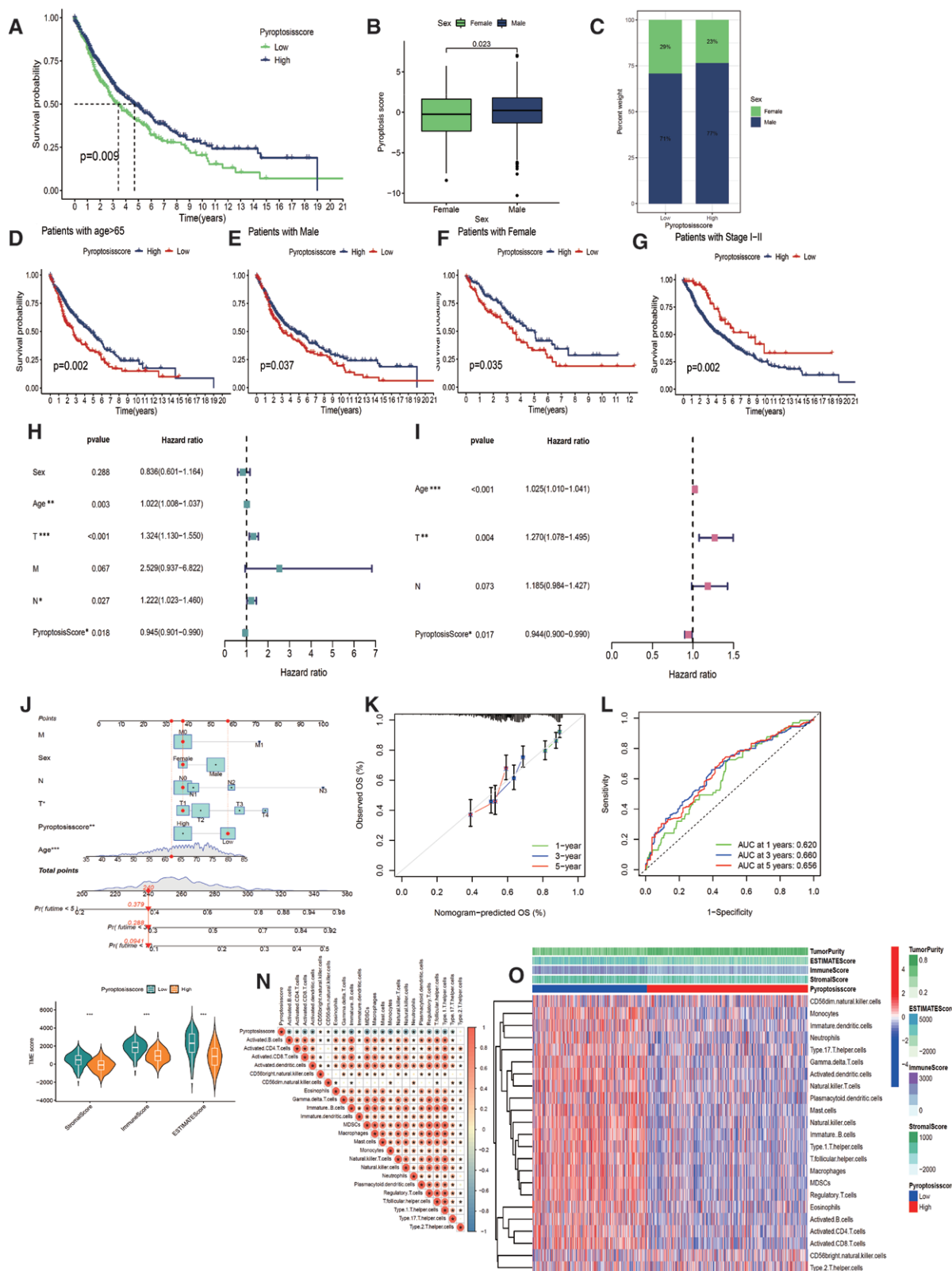
Figure 5. Pyroptosis score association with LUSC clinical characteristics and TME immune infiltration. (A) Kaplan–Meier curves showed overall survival of the patients associated with different pyroptosis scores (Log-rank test, P = .009). (B) The correlation of pyroptosis score with the gender of patients. (C) The proportion of patients' gender in the pyroptosis score groups. (D–G) Overall survival curves for the pyroptosis score groups based on patients' clinical characteristics such as age >65 (D, Log-rank test, P = .002), male (E, Log-rank test, P = .037), (F, Log-rank test, P = .035) and stage I–II (G, Log-rank test, P = .002). Red: low pyroptosis score; Blue: high pyroptosis score. (H–I) Hazard ratio and P-value of the constituents involved in the univariate (H) and multivariate (I) Cox regression considering clinical characteristics and pyroptosis scores in LUSC. (J–L) A nomogram to predict the 1-, 3-, and 5-year overall survival rate of patients with LUSC (J). An example was shown in the nomogram as red dots representing a patient with LUSC who was a 62-year-old female with T1N0M0 stage and a low pyroptosis score. She was calculated as 240 points with a survival time of 37.90% probability and <5 years, 28.8% probability and <3 years, and 9.41% probability and <1 year. Calibration curves for the overall survival nomogram model (K) and ROC curves for the predictive efficiency of the pyroptosis score (L). (M) The stromal score, immune score, and ESTIMATE score of different pyroptosis score groups were analyzed and plotted. *P < .05, **P < .01, ***P < .001. (N–O) Correlation between pyroptosis scores and the immune infiltration cells using Spearman analysis (N) and a heatmap visualizing the abundance of tumor-infiltrating lymphocytes (O). The negative correlation was marked with blue and the positive correlation was marked with red. ESTIMATE scores such as immune score, stromal score, and tumor purity are shown in annotations above. LUSC = lung squamous cell carcinoma, ROC = receiver operating characteristic, TME = tumor immune microenvironment.
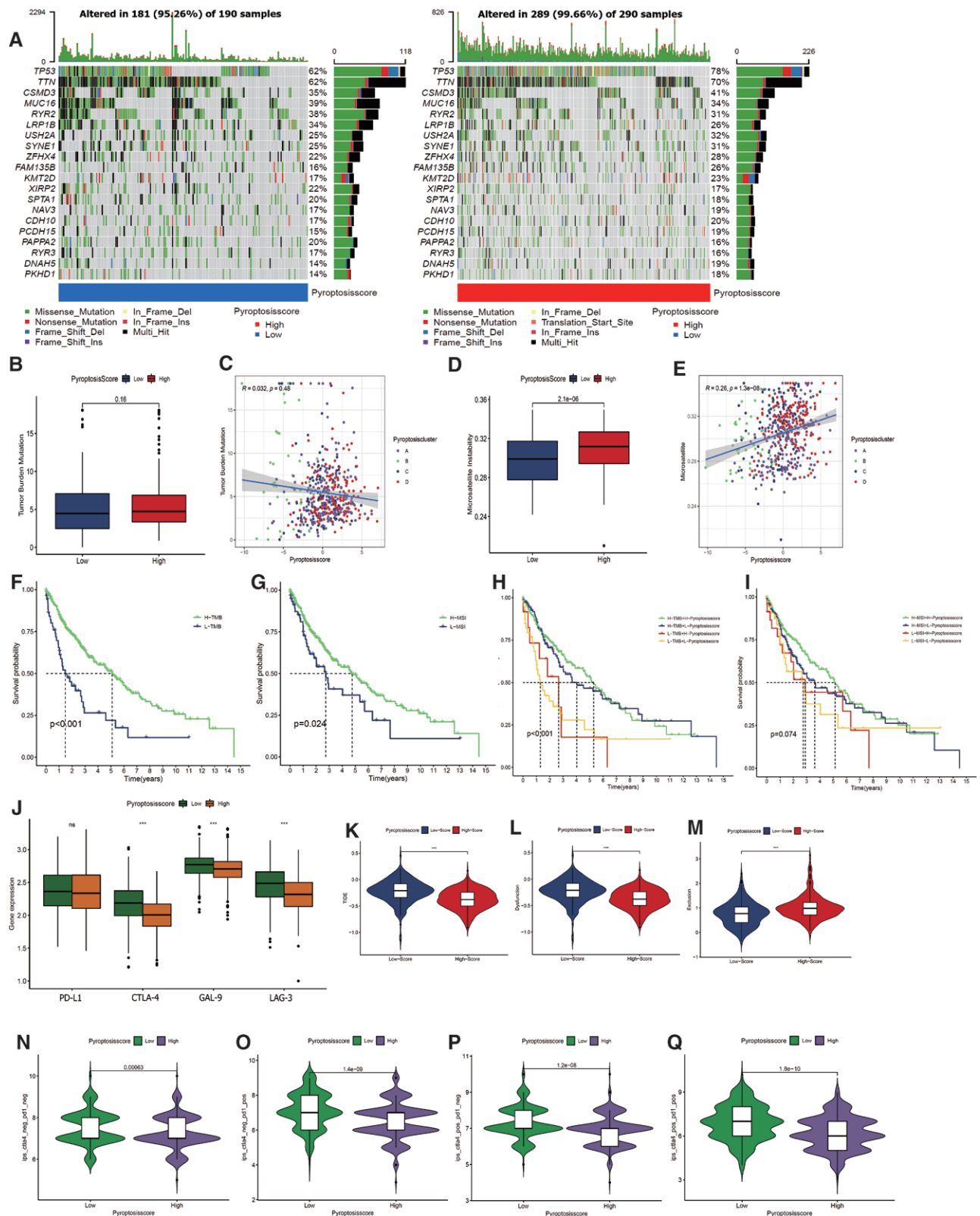
Figure 6. The role of pyroptosis score in predicting ICI immunotherapy benefits. (A) Mutational landscape of frequently mutated genes in TCGA-LUSC stratified by low (left) and high pyroptosis scores (right). Each column represents individual patients. The number on the right indicates the mutation frequency in each gene. (B–E) The relationship between pyroptosis score and high or low TMB (B), as well as MSI (D). The correlation of pyroptosis score with TMB and MSI in different pyroptosis clusters are also shown in C and E. (F–I) Overall survival curves for the TMB (F) and MSI (G) and the combination of TMB with pyroptosis scores (H), as well as MSI with pyroptosis scores (I) based on patients in TCGA-LUSC cohort. (J) Differential expression of immune checkpoints in high or low pyroptosis score group. *$P < .05$, **$P < .01$, ***$P < .001$. (K–M) The relative distribution of TIDE was compared between pyroptosis score groups in TCGA-LUSC cohort (K) simultaneously calculating immune dysfunction (L) and exclusion (M). (N–Q) The relative distribution of IPS was compared between pyroptosis score subgroups in TCGA-LUSC cohort representing patients receiving no ICI therapy (N), anti-PD-1 therapy (O), anti-CTLA-4 therapy (P), and anti-PD-1/CTLA-4 therapy (Q). ICI = immune checkpoint inhibitor, IPS = immunophenoscore, LUSC = lung squamous cell carcinoma, MSI = microsatellite instability, TCGA = The Cancer Genome Atlas, TIDE = tumor immune dysfunction and exclusion, TMB = tumor mutational burden.

a significant difference was observed between the pyroptosis score subgroups (*P* < .001). Once patients received one of these 2 ICI therapies, patients in low pyroptosis score group therapeutically benefited more than those in high score group (anti-CTLA-4: *P* < .001; anti-PD-L1: *P* < .001; anti-CTLA-4 and anti-PD-L1: *P* < .001; Fig. 6N–Q). Taken together, our results strongly suggest that the pyroptosis score might predict the response to immunotherapies.

3.7. Clinical experimental validation

We performed IHC and RNA-seq validation of the clinical specimens following the steps described above. IHC results showed that ABCF3, IGSF11, P2RY6, and SOX2 proteins were expressed at higher levels in LUSC tissues than in normal tissues, whereas FGFR2 expression was diminished in tumors (Fig. 7A–E). In the Human Protein Atlas (HPA) database validation, ACSL5, DVL3, LAMC2, and SPASR showed higher expression in LUSC samples, whereas NTS and SOX21 showed no evident difference in expression between tumor and normal tissues (see Figure S3A–F, Supplemental Digital Content 3, http://links.lww.com/MD/H205, which shows IHC images of candidate genes in HPA).

In our RNA-seq database validation, only *ACSL5*, *FGFR2*, *LAMC2*, and *P2RY6* showed differential expression between tumor and normal tissues, among which *ACSL5* (*P* < .01) and *P2RY6* (*P* < .001) were upregulated, whereas *FGFR2* (*P* < .01) and *LAMC2* (*P* < .01) were downregulated in LUSC tissues (Fig. 7F–I, see Figure S3G–N, Supplemental Digital Content 3, http://links.lww.com/MD/H205, which shows expression levels

of candidate genes). Interestingly, the *LAMC2* levels found here were not consistent with the IHC results, which might be explained by limited sample size and gene regulation.

4. Discussion

Chronic inflammation is a prolonged immune response that contributes to the pathogenesis of cancer.[37] As a lytic, pro-inflammatory type of cell death, pyroptosis leads to inflammation induced by various stimuli and plays a pivotal role in many cancers.[38] Although mounting studies have emphasized the reprogramming roles of pyroptosis in the tumor immune microenvironment, the general TME features facilitated by pyroptosis factors have not been given a comprehensive insight.[39,40] Therefore, exploring the alterations in the immune microenvironment and its association with pyroptosis will provide an in-depth understanding of the LUSC inflammation response and offer an innovative immunotherapy strategy.

In our study, 4 pyroptosis-related clusters, characterized by tumor PD-L1 expression and immune infiltration profusion, were discovered. Pyroptosis-ClusterA is distinguished by restrained PD-L1 expression with TIL, indicating that non-functional immune cell infiltration might be induced by certain suppressors involved in promoting immune tolerance. Pyroptosis-ClusterC is obviously characterized by an ameliorated PD-L1 level together with abundant TILs, representing an active immune response. The pyroptosis-ClusterD is characterized by PD-L1 negativity with no TIL corresponding to an immune-ignorant phenotype. Pyroptosis-ClusterB could be classified as intrinsic induction immunocyte
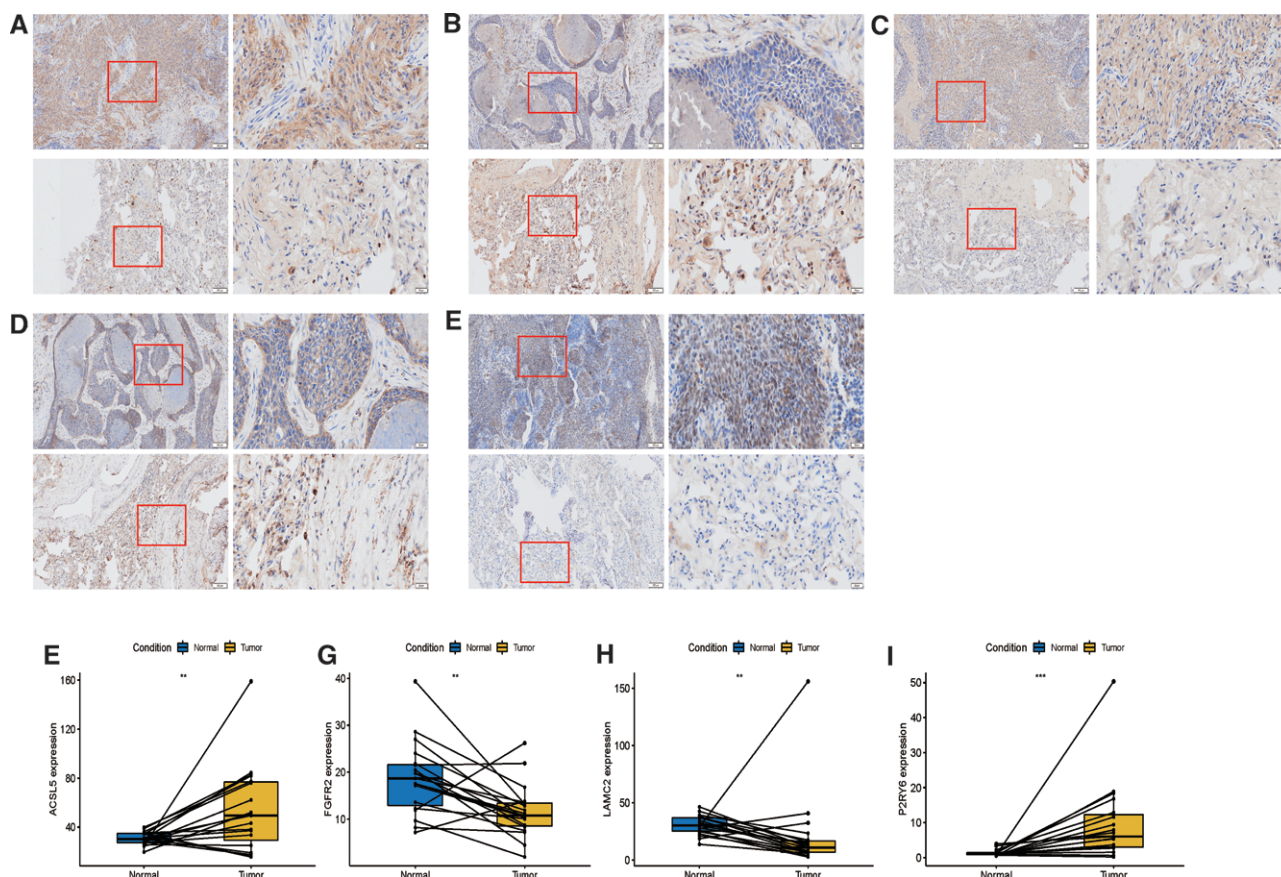

Figure 7. Validation of candidate gene expression in clinical tissue samples. (A–E) Representative images of IHC staining in clinical samples. (A) ABCF3; (B) FGFR2; (C) IGSF11; (D) P2RY6; (E) SOX2. The upper row of each figure represents tumor tissues and the lower row represents normal tissues. Scale bar = 20 μm: magnification = ×10; Scale bar = 100 μm: magnification = ×40. (F–I) The expression levels of ACSL5 (F), FGFR2 (G), LAMC2 (H) and P2RY6 (I) in normal and LUSC tissues in our own RNA-seq database. **P* < .01, ***P* < .001. IHC = immunohistochemistry, LUSC = lung squamous cell carcinoma, ns = not significant.

infiltration with diminished tumor purity. Specifically, studies have shown that this type of TME classification might be more commonly accompanied by oncogenic mutation-driven mechanism.[41,42] We identified that typical oncogenic pathways such as P53 signaling, MAPK signaling, Wnt signaling, and ErbB signaling pathways are significantly attenuated in the pyroptosis-ClusterB, which might be interpreted by mutations of the genes involved in the pathway. The state of "immunological ignorance" (pyroptosis-ClusterD) and "immune exclusion" (pyroptosis-ClusterB), which could be termed an immunologically quiet TME, has been verified to be associated with a poor response to ICIs.[43] The immune phenotype of pyroptosis-ClusterC supported the potential benefits of a single anti-PD-L1 blockade, which could be explained by its pre-existing intratumoral T cells being turned off by PD-L1.[44] Moreover, we found that pyroptosis-related regulators exhibit different expression levels among these 4 clusters owing to various heterogeneities, which showed positive correlations with immune cell infiltration abundance. Wang et al[45] conducted single-cell sequencing and discovered that pyroptosis-inducible therapy increases NK, CD4+ T, and CD8+ T cell infiltration in breast cancer. Meanwhile, pyroptosis can eliminate the populations of monocytes, neutrophils, and myeloid-derived suppressor cells, as well as induce the polarization of macrophage M1.[45] In particular, the tumor suppressive effect of GSDME, a well-known non-canonical inflammasome member, was observed in immune-deficient mice that lack a pyroptosis-dependent antitumor immune response.[46,47] Moreover, GSDME expression was found to increase antitumor immunity by enhancing the function and abundance of NK lymphocytes to prevent immune evasion of tumor.[48,49] Consistent with previous studies, our results demonstrated that GSDME expression and NK lymphocyte infiltration are simultaneously restrained in pyroptosis-ClusterB, indicating the lack of non-canonical pyroptosis inflammasome pathways and possible immune evasion in ClusterB. Apart from the mechanism of directly eradicating tumor cells, pyroptosis may also overcome immunosuppression and reactivate adaptive antitumor immune responses.[50] According to the findings, we conjecture that pyroptosis-related genes might provide an opportunity to turn "cold" tumor to "hot" and overcome the immune-desert phenotype of TME.

We identified 17 DEGs from 4 pyroptosis subgroups, and these 17 genes are significantly enriched in the cell differentiation process and intracellular transport, which might be considered pyroptosis-related gene signatures. Based on these 17 pyroptosis signature genes, 3 transcriptomic subtypes were clustered by consensus, which provide an accurate long-term survival prediction. To further guide individual treatments for patients with LUSC, we developed a pyroptosis scoring method to quantify the heterogeneity between distinct pyroptosis patterns. Our results verified that immune-responsive and immune-exclusion phenotypes showed a lower pyroptosis score, whereas immune-non-functional and immune-ignorant phenotypes mainly exhibited a higher pyroptosis score. In addition, the pyroptosis score could effectively discriminate between pyroptosis clusters and gene signature clusters, which emphasized that pyroptosis scores could represent patients with different pyroptosis regulation patterns. A low pyroptosis score is remarkably correlated with worse clinical traits and worse prognosis. The pyroptosis score is positively associated with MSI and enhanced the ability to predict LUSC prognosis when combined with TMB, suggesting that the pyroptosis score could provide sufficient information on patient outcomes. Further analysis was performed to evaluate the mutation frequencies of the onco-driver genes to gain a better understanding of pyroptosis scores in cancer progression. We found that *MUC16* and *RYR2* mutations were more frequent in low score subgroup, whereas *TP53*, *TTN*, and *CSMD3* had a novel mutation rate in this high score subgroup. Previous studies have shown that *MUC16* mutations are associated with higher immune response rates, prolonged OS, and better anti-PD-L1 response, especially in NSCLC.[51] The *RYR2* mutational

signature was correlated with the presence of dendritic cells, which were more efficient in stimulating T-cell proliferation.[52] It has been reported that the *RYR2* mutation is associated with a favorable outcome and immune infiltration in high PD-L1-expressing tumors.[52] *TP53* and *TTN* are widespread mutated genes in LUSC, and both mutations could serve as predictors of improved outcomes in response to ICI therapy.[52] The *CSMD3* mutation was found to be related to resistance to etoposide in small-cell lung cancer.[53] However, limited evidence exists regarding the role of *CSMD3* mutations in the immune regulation of cancer. These pyroptosis-related oncogene mutations were confirmed in our study to be linked to immune activity, signifying the potential role of pyroptosis in the immunogenomic features of LUSC.

Using the TIDE and IPS methods, the vigorous estimation capacity of the pyroptosis score in ICI therapy response was confirmed in our analysis. TME infiltration results demonstrated that the pyroptosis score was valuable for immunotherapy response, and stimulated immune cell infiltration led to a low pyroptosis score and better response to ICI therapy. ICI treatment efficacy is limited, and approximately one-third of patients are responsive.[35] For tumors deemed "cold," ICIs could efficiently kill cold tumor cells with the concomitant induction of pyroptosis.[54] Zhou et al[1] found that granzyme A could trigger tumor cell pyroptosis through the cleavage of GSDMB, which could play a pivotal role in cytotoxin-induced pyroptosis. *GSDMD* is upregulated in activated CD8+ T cells, and its downregulation might reduce its cytolytic capacity in lung cancer.[55,56] A synergistic effect of ICI- and GSDM family-mediated cell membrane defects induces intense inflammatory responses and massive infiltration of lymphocytes, which positively form a feedback to induce pyroptosis.[46,57]

Although we included most of the pyroptosis-related genes as well as all GEO datasets containing LUSC samples and performed multi-perspective analysis, our study still has limitations. First, our study did not show a correlation between the pyroptosis score and clinicopathological characteristics, such as smoking status, *KRAS/EGFR/STK11* mutations, and distant metastasis, which require more extensive information to improve accuracy. Second, no significant results were implied between pyroptosis score and TMB of LUSC in TCGA cohorts, which still needs validation to confirm their relationship. In addition, all databases utilized in this study were retrospective, and a well-designed prospective cohort of patients with LUSC receiving immunotherapy is recommended.

In this study, we estimated the pyroptosis regulatory patterns of 833 LUSC samples based on 41 pyroptosis-related genes and classified them according to specific TME infiltration features. Our integrated analysis provides a deeper understanding of the role of pyroptosis in cancer immunity regulation, and precise evaluation of the pyroptosis signature will enhance our prediction of LUSC prognosis and ICI treatment response.

Author contributions

Conceptualization: Xiaheng Deng, Liang Chen, Yu Luo.
Data curation: Xiaheng Deng.
Formal analysis: Xiaheng Deng, Zhibo Wang, Zhihua Li.
Funding acquisition: Liang Chen, Yu Luo.
Investigation: Xiaheng Deng, Zhibo Wang, Zhihua Li.
Methodology: Zhibo Wang, Zhihua Li, Yu Luo.
Resources: Yu Luo.
Software: Zhihua Li, Yu Luo.
Supervision: Liang Chen, Yu Luo.
Visualization: Zhihua Li.
Writing – original draft: Xiaheng Deng, Zhihua Li.
Writing – review & editing: Liang Chen, Yu Luo.

References

[1] Zhou Z, He H, Wang K, et al. Granzyme A from cytotoxic lymphocytes cleaves GSDMB to trigger pyroptosis in target cells. Science. 2020;368:eaaz7548.

[2] Shi J, Zhao Y, Wang K, et al. Cleavage of GSDMD by inflammatory caspases determines pyroptotic cell death. Nature. 2015;526:660–5.

[3] Kayagaki N, Stowe IB, Lee BL, et al. Caspase-11 cleaves gasdermin D for non-canonical inflammasome signalling. Nature. 2015;526:666–71.

[4] Julien O, Wells JA. Caspases and their substrates. Cell Death Differ. 2017;24:1380–9.

[5] Wu J, Lin S, Wan B, et al. Pyroptosis in liver disease: new insights into disease mechanisms. Aging Dis. 2019;10:1094–108.

[6] Song X, Cui Z, He J, et al. kappaopioid receptor agonist, U50488H, inhibits pyroptosis through NLRP3 via the Ca(2+)/CaMKII/CREB signaling pathway and improves synaptic plasticity in APP/PS1 mice. Mol Med Rep. 2021;24:529.

[7] Xu YJ, Zheng L, Hu YW, et al. Pyroptosis and its relationship to atherosclerosis. Clin Chim Acta. 2018;476:28–37.

[8] Xia X, Wang X, Cheng Z, et al. The role of pyroptosis in cancer: pro-cancer or pro-"host"? Cell Death Dis. 2019;10:650.

[9] Wang M, Jiang S, Zhang Y, et al. The Multifaceted roles of pyroptotic cell death pathways in cancer. Cancers (Basel). 2019;11:1313.

[10] Ye Y, Dai Q, Qi H. A novel defined pyroptosis-related gene signature for predicting the prognosis of ovarian cancer. Cell Death Discov. 2021;7:71.

[11] Yin D, Lu X, Su J, et al. Long noncoding RNA AFAP1-AS1 predicts a poor prognosis and regulates non-small cell lung cancer cell proliferation by epigenetically repressing p21 expression. Mol Cancer. 2018;17:92.

[12] Du P, Hu T, An Z, et al. In vitro and in vivo synergistic efficacy of ceritinib combined with programmed cell death ligand-1 inhibitor in anaplastic lymphoma kinase-rearranged non-small-cell lung cancer. Cancer Sci. 2020;111:1887–98.

[13] Le DT, Durham JN, Smith KN, et al. Mismatch repair deficiency predicts response of solid tumors to PD-1 blockade. Science. 2017;357:409–13.

[14] Binnewies M, Roberts EW, Kersten K, et al. Understanding the tumor immune microenvironment (TIME) for effective therapy. Nat Med. 2018;24:541–50.

[15] Tumeh PC, Harview CL, Yearley JH, et al. PD-1 blockade induces responses by inhibiting adaptive immune resistance. Nature. 2014;515:568–71.

[16] Chen N, Fang W, Zhan J, et al. Upregulation of PD-L1 by EGFR activation mediates the immune escape in EGFR-driven NSCLC: implication for optional immune targeted therapy for NSCLC patients with EGFR mutation. J Thorac Oncol. 2015;10:910–23.

[17] Herbst RS, Soria JC, Kowanetz M, et al. Predictive correlates of response to the anti-PD-L1 antibody MPDL3280A in cancer patients. Nature. 2014;515:563–7.

[18] Teng MW, Ngiow SF, Ribas A, et al. Classifying cancers based on T-cell infiltration and PD-L1. Cancer Res. 2015;75:2139–45.

[19] Kroemer G, Galluzzi L, Kepp O, et al. Immunogenic cell death in cancer therapy. Annu Rev Immunol. 2013;31:51–72.

[20] Duan Q, Zhang H, Zheng J, et al. Turning cold into hot: firing up the tumor microenvironment. Trends Cancer. 2020;6:605–18.

[21] Li J, Byrne KT, Yan F, et al. Tumor cell-intrinsic factors underlie heterogeneity of immune cell infiltration and response to immunotherapy. Immunity. 2018;49:178–193.e7.

[22] Zhang Z, Zhang Y, Xia S, et al. Gasdermin E suppresses tumour growth by activating anti-tumour immunity. Nature. 2020;579:415–20.

[23] Ershaid N, Sharon Y, Doron H, et al. NLRP3 inflammasome in fibroblasts links tissue damage with inflammation in breast cancer progression and metastasis. Nat Commun. 2019;10:4375.

[24] Gao J, Qiu X, Xi G, et al. Downregulation of GSDMD attenuates tumor proliferation via the intrinsic mitochondrial apoptotic pathway and inhibition of EGFR/Akt signaling and predicts a good prognosis in nonsmall cell lung cancer. Oncol Rep. 2018;40:1971–84.

[25] Wilkerson MD, Yin X, Hoadley KA, et al. Lung squamous cell carcinoma mRNA expression subtypes are reproducible, clinically important, and correspond to normal cell types. Clin Cancer Res. 2010;16:4864–75.

[26] Rousseaux S, Debernardi A, Jacquiau B, et al. Ectopic activation of germline and placental genes identifies aggressive metastasis-prone lung cancers. Sci Transl Med. 2013;5:186ra166.

[27] Botling J, Edlund K, Lohr M, et al. Biomarker discovery in non-small cell lung cancer: integrating gene expression profiling, meta-analysis, and tissue microarray validation. Clin Cancer Res. 2013;19:194–204.

[28] Parra ER, Behrens C, Rodriguez-Canales J, et al. Image analysis-based assessment of PD-L1 and tumor-associated immune cells density supports distinct intratumoral microenvironment groups in non-small cell lung carcinoma patients. Clin Cancer Res. 2016;22:6278–89.

[29] Zhou H, Zhang H, Shi M, et al. A robust signature associated with patient prognosis and tumor immune microenvironment based on immune-related genes in lung squamous cell carcinoma. Int Immunopharmacol. 2020;88:106856.

[30] Mayakonda A, Lin DC, Assenov Y, et al. Maftools: efficient and comprehensive analysis of somatic variants in cancer. Genome Res. 2018;28:1747–56.

[31] Karki R, Kanneganti TD. Diverging inflammasome signals in tumorigenesis and potential targeting. Nat Rev Cancer. 2019;19:197–214.

[32] Charoentong P, Finotello F, Angelova M, et al. Pan-cancer immunogenomic analyses reveal genotype-immunophenotype relationships and predictors of response to checkpoint blockade. Cell Rep. 2017;18:248–62.

[33] Yoshihara K, Shahmoradgoli M, Martinez E, et al. Inferring tumour purity and stromal and immune cell admixture from expression data. Nat Commun. 2013;4:2612.

[34] Alba AC, Agoritsas T, Walsh M, et al. Discrimination and calibration of clinical prediction models: users' guides to the medical literature. JAMA. 2017;318:1377–84.

[35] Jiang P, Gu S, Pan D, et al. Signatures of T cell dysfunction and exclusion predict cancer immunotherapy response. Nat Med. 2018;24:1550–8.

[36] Wang C, Yin R, Dai J, et al. Whole-genome sequencing reveals genomic signatures associated with the inflammatory microenvironments in Chinese NSCLC patients. Nat Commun. 2018;9:2054.

[37] Crusz SM, Balkwill FR. Inflammation and cancer: advances and new agents. Nat Rev Clin Oncol. 2015;12:584–96.

[38] Tan Y, Chen Q, Li X, et al. Pyroptosis: a new paradigm of cell death for fighting against cancer. J Exp Clin Cancer Res. 2021;40:153.

[39] Wu D, Wang S, Yu G, et al. Cell death mediated by the pyroptosis pathway with the aid of nanotechnology: prospects for cancer therapy. Angew Chem Int Ed Engl. 2021;60:8018–34.

[40] Zhang Z, Zhang Y, Lieberman J. Lighting a fire: can we harness pyroptosis to ignite antitumor immunity? Cancer Immunol Res. 2021;9:2–7.

[41] Chen N, Fang W, Lin Z, et al. KRAS mutation-induced upregulation of PD-L1 mediates immune escape in human lung adenocarcinoma. Cancer Immunol Immunother. 2017;66:1175–87.

[42] Toki MI, Mani N, Smithy JW, et al. Immune marker profiling and programmed death ligand 1 expression across NSCLC mutations. J Thorac Oncol. 2018;13:1884–96.

[43] Kargl J, Zhu X, Zhang H, et al. Neutrophil content predicts lymphocyte depletion and anti-PD1 treatment failure in NSCLC. JCI Insight. 2019;4:e13050.

[44] Chi A, He X, Hou L, et al. Classification of non-small cell lung cancer's tumor immune micro-environment and strategies to augment its response to immune checkpoint blockade. Cancers (Basel). 2021;13:2924.

[45] Wang Q, Wang Y, Ding J, et al. A bioorthogonal system reveals antitumour immune function of pyroptosis. Nature. 2020;579:421–6.

[46] Erkes DA, Cai W, Sanchez IM, et al. Mutant BRAF and MEK inhibitors regulate the tumor immune microenvironment via pyroptosis. Cancer Discov. 2020;10:254–69.

[47] Li L, Jiang M, Qi L, et al. Pyroptosis, a new bridge to tumor immunity. Cancer Sci. 2021;112:3979–94.

[48] Kumar S, Calianese D, Birge RB. Efferocytosis of dying cells differentially modulate immunological outcomes in tumor microenvironment. Immunol Rev. 2017;280:149–64.

[49] Werfel TA, Cook RS. Efferocytosis in the tumor microenvironment. Semin Immunopathol. 2018;40:545–54.

[50] Tang R, Xu J, Zhang B, et al. Ferroptosis, necroptosis, and pyroptosis in anticancer immunity. J Hematol Oncol. 2020;13:110.

[51] Zhang L, Han X, Shi Y. Association of MUC16 mutation with response to immune checkpoint inhibitors in solid tumors. JAMA Netw Open. 2020;3:e2013201.

[52] Cimas FJ, Manzano A, Baliu-Pique M, et al. Genomic mapping identifies mutations in RYR2 and AHNAK as associated with favorable outcome in basal-like breast tumors expressing PD1/PD-L1. Cancers (Basel). 2020;12:2243.

[53] Qiu Z, Lin A, Li K, et al. A novel mutation panel for predicting etoposide resistance in small-cell lung cancer. Drug Des Devel Ther. 2019;13:2021–41.

[54] Topalian SL, Taube JM, Anders RA, et al. Mechanism-driven biomarkers to guide immune checkpoint blockade in cancer therapy. Nat Rev Cancer. 2016;16:275–87.

[55] Xi G, Gao J, Wan B, et al. GSDMD is required for effector CD8(+) T cell responses to lung cancer cells. Int Immunopharmacol. 2019;74:105713.

[56] Zhang J, Chen Y, He Q. Distinct characteristics of dasatinib-induced pyroptosis in gasdermin E-expressing human lung cancer A549 cells and neuroblastoma SH-SY5Y cells. Oncol Lett. 2020;20:145–54.

[57] Gao Y, Zhang H, Zhou N, et al. Methotrexate-loaded tumour-cell-derived microvesicles can relieve biliary obstruction in patients with extrahepatic cholangiocarcinoma. Nat Biomed Eng. 2020;4:743–53.